Journal of Enhanced Heat Transfer, 26(2):127–143 (2019)

ENHANCED CONDUCTION AND POOL BOILING HEAT TRANSFER ON SINGLE-LAYER GRAPHENE-COATED SUBSTRATES

*Ricardo Diaz & Zhixiong Guo**

Department of Mechanical and Aerospace Engineering, Rutgers, The State University of New Jersey, Piscataway, NJ 08854, USA

*Address all correspondence to: Zhixiong Guo, Department of Mechanical and Aerospace Engineering, Rutgers, The State University of New Jersey, Piscataway, NJ 08854, USA, E-mail: guo@jove.rutgers.edu

Original Manuscript Submitted: 9/7/2018; Final Draft Received: 9/10/2018

Molecular dynamics simulations were employed to understand the improved thermal conductivity and water boiling heat transfer characteristics of adding single-layer graphene (SLG) to substrates. The 100, 110, and 111 planes of Cu, Ni, Pt, and Si were selected for study based on common heat transfer and graphene-compatible materials. Vibrational density of states data were analyzed in order to view heat flux trends. After equilibration at 300 K the temperature was increased to 400 K for 3 ns to induce nucleate boiling ($\sim$ 27 K wall superheat). It was found that the addition of SLG greatly improved the overall thermal conductivity of the composite substrate, with increases in the one to two orders of magnitude range. The temperature gradients for SLG-coated substrates were found to be much lower than bare substrates. Nanoscale boiling curves were produced. The CuG100 case shows a 14% increase in critical heat flux (CHF) ($\sim 0.36\ GW/m^2$) over the Cu100 case, and the PtG100 shows a 9% increase ($\sim 0.48\ GW/m^2$) over the Pt100 case. The SLG-coated substrates also required less superheat to achieve the CHF condition.

KEY WORDS: *boiling heat transfer, thermal conductivity, graphene, critical heat flux, nanoscale heat transfer, molecular dynamics simulation*

1. INTRODUCTION

As electronics and electromechanical devices continue to require increased power capabilities with reduced spatial profiles, it is important to explore a multitude of methods for removing high heat fluxes (Jaikumar et al., 2017). The micro- and nanotechnology fields also contribute to this need, as electrical processes at these very small scales naturally result in very high power densities. To this end boiling heat transfer has long been studied due to its ability to remove high heat flux through phase change (Gheltaghy et al., 2018; Kubo et al., 2017; Shatto and Peterson, 2017).

Pool boiling specifically is attractive due to its passive nature, resulting in reduced system complexity and ease of implementation. However, the mechanisms and many factors involved in these boiling scenarios are still unclear and are being investigated. In order to form a better

NOMENCLATURE

C	numerical constant (eV· F/C^2)	r_c	cutoff radius for particle interaction calculations (Å)
D	VDOS, dimensionless	r_i	position vector of atom i (Å)
e_i	energy of atom i (eV)	S	VDOS overlap, dimensionless
E	potential energy (eV)	S_i	stress of atom I (eV/Å^3)
f	frequency (Hz)	t	time (ps)
f_i	force vector of atom i (eV/Å)	T	temperature (K)
J	heat flux [eV/(Å^2 · ps)]	v_i	velocity of atom i (Å/ps)
k	thermal conductivity [eV/(Å·K·ps)]	V	volume (Å^3)
k_B	Boltzmann constant (eV/K)	ϵ	Lennard-Jones potential well depth (eV)
q	atomic charge (C)	ϵ_0	dielectric constant (F/Å)
r	interparticle distance (Å)	σ	Lennard-Jones characteristic length (Å)

understanding of boiling heat transfer on the nanoscale, molecular dynamics (MD) simulations are a useful method to gain insights at the molecular level, because carrying out experiments on a scale this small is difficult. MD simulations can provide good qualitative and quantitative data for configurations that are prohibitive to recreate experimentally, or that are not yet possible to create due to technological or financial constraints. MD also overcomes the limitations of classical theories based on continuum mechanics and thermodynamics, and allows for simple and flexible control of many variables such as pressure, temperature, heat flux, etc.

A method of improving heat transfer that has garnered much attention in the recent past is the use of graphene. Graphene has a host of favorable properties, including very high thermal conductance (Nika et al., 2009) and effective thermal rectification (Ouyang et al., 2010). The effect of geometry and temperature of metal-graphene composites has been investigated via MD simulation (Chang et al., 2012), showing that interface conductance tends to decrease as the number of graphene layers is increased. The thermal resistance at a water-graphene interface was also simulated (Alexeev et al., 2015), showing that the Kapitza resistance decreased with increasing number of graphene layers, and was also dependent on the density stratification of the adjacent water block. More recently, some pool boiling experiments have shown an increase in heat transfer when using graphene-coated substrates. Seo et al. (2015) showed a 9% increase in critical heat flux (CHF) for a nonporous graphene-coated ITO (indium tin oxide) surface over bare ITO, while porous graphene-coated ITO increased CHF by 90%. Similarly, Jaikumar et al. (2017) showed both CHF and a heat transfer coefficient of over 40% when comparing water boiling on a copper versus graphene and graphene oxide-coated copper.

Previous studies have looked at the effects of different substrate topologies, including flat substrates and those topped with nanostructures Diaz and Guo (2017a). Nanopillar height effect on evaporation was investigated (Morshed et al., 2011), showing that the evaporation rate increased with nanostructure height, and that the liquid-film separation temperature during explosive boiling also increased. Seyf and Zhang (2013) showed a similar result with increasing spherical nanoparticle size, and also observed smaller droplet sizes during explosive boiling as the nanoparticle diameters increased. The effect of wettability on a nanostructured substrate was

investigated by Diaz and Guo (2017b), showing that CHF tends to increase with the hydrophilicity of both the base wall and nanostructures.

While some pool boiling experiments involving graphene-coated substrates have been carried out, very few, if any, simulations have explored this scenario on the nanoscale. In this study, metallic substrates like copper, nickel, and platinum, and the semiconductor silicon are topped with single-layer graphene, and system temperatures are raised to induce both nucleate and explosive boiling of water. Such substrates have favorable thermal properties and have been used to grow graphene in the past (Chang et al., 2012; Choi et al., 2010). These materials are often used in electronic chips and other high-power devices due to their thermal properties (among others), and enhancing these properties is often a method used to improve system performance. For the metal substrates there is also the possibility of growing large area graphene films via chemical vapor deposition (Dahal and Batzill, 2014). Simulation of these different scenarios allows for comparison of many system attributes, including liquid density, heat flux, substrate thermal conductivity, and vibrational density of states, to gain insight into the heat transfer mechanisms of these small-scale systems.

2. SIMULATION METHODS

The simulation domain shown in Fig. 1 consists of a metal substrate topped with a single layer of graphene, over which the liquid water rests. Water vapor fills the rest of the simulation domain. The domain is roughly $49 \times 46 \times 210$ angstroms (Å), although slight changes to each dimension were made in certain cases to accommodate the varying substrate lattice parameters. To prevent finite size effects the domain is periodic in both the positive and negative x and y directions, while the upper z boundary is a fixed, reflective, adiabatic boundary. Each substrate consisted of five monolayers, where the bottom monolayer was held immobile to act as a lower z direction boundary, and the second layer was used for thermostatting purposes. Based on previous work

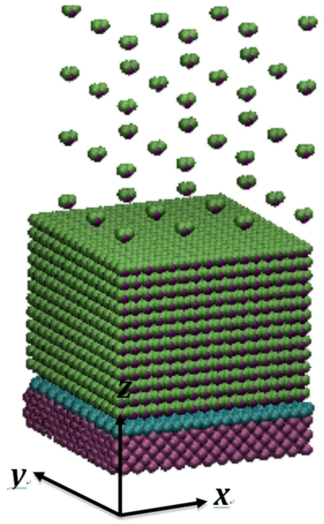

FIG. 1: Setup of simulation domain

(Morshed et al., 2011), the upper three layers were deemed to be enough for use as conduction layers to heat the water above. The Cu, Ni, and Pt were arranged in an fcc lattice structure, with densities of 8.96 g/cm^3, 8.91 g/cm^3, and 21.46 g/cm^3, respectively. The Si substrate was arranged in a diamond cubic structure with a density of 2.33 g/cm^3.

For each substrate, boiling simulations were run using the 100, 110, and 111 planes in order to test conductivity and compatibility with the graphene layer. Each plane has a different lattice mismatch with graphene as well as a slightly different substrate-graphene separation distance, which could affect overall heat transfer. The number of substrate atoms ranged from 720 to 2185 atoms. Table 1 shows the simulation domain dimensions and number of substrate atoms for each case. In this study cases are referred to by the substrate material, lattice plane, and graphene layer (e.g., CuG100); in the cases without graphene used for comparison purposes, only the substrate and plane are marked (i.e., Cu100). Eight hundred eighty graphene atoms were arranged above the main substrate with the standard hexagonal (honeycomb) lattice, with a 2.46-Å lattice constant.

Twelve monolayers of liquid water (forming a 36-Å-thick film) were initially placed above the graphene layer with water vapor molecules filling the rest of the domain, totaling 3192 molecules. The extended simple point charge (SPC/E) water model was employed, which uses a 1-Å bond length, 109.47° HOH bond angle, –0.8476e oxygen charge, and 0.4238e hydrogen charge. The SHAKE algorithm was used to maintain the molecule geometry, while a PPPM solver with 10^{-4} accuracy was used to compute long-range Coulombic interactions. All simulations were conducted using LAMMPS software (version 31, Mar 2017), an open-source classical MD code based on Plimpton's work (Plimpton, 1995), while visualization was performed with VMD v1.9.1 (Humphrey et al., 1996).

The interactions between graphene and hydrogen molecules were modeled using the AIREBO potential (Stuart et al., 2000) with a 10.2-Å cutoff. Interactions between Si atoms were modeled using the three-body Stillinger-Weber potential with a cutoff of 3.8 Å, which works well for atoms arranged in the diamond cubic lattice structure (Si, Ge, etc.). The remaining interactions were modeled using the standard 12-6 Lennard-Jones (LJ) potential with an additional

TABLE 1: System dimensions and substrate configurations

Case	Dimensions (Å)	# Substrate Atoms
CuG100	$50.6 \times 47.0 \times 211.0$	1820
CuG110	$51.3 \times 46.8 \times 208.2$	1359
CuG111	$50.6 \times 46.8 \times 210.5$	2128
NiG100	$49.3 \times 46.8 \times 210.5$	1890
NiG110	$49.3 \times 47.4 \times 207.9$	1330
NiG111	$49.6 \times 46.8 \times 211.9$	2185
PtG100	$50.0 \times 47.1 \times 211.5$	1560
PtG110	$51.0 \times 46.8 \times 208.6$	1105
PtG111	$49.2 \times 48.6 \times 213.3$	1854
SiG100	$49.2 \times 46.8 \times 208.2$	720
SiG110	$49.2 \times 46.8 \times 211.3$	1080
SiG111	$49.2 \times 46.8 \times 209.5$	1040

term to take Coulombic interactions into account. The full potential E is given by

$$E = 4\epsilon_{LJ}\left[\left(\frac{\sigma}{r}\right)^{12} - \left(\frac{\sigma}{r}\right)^{6}\right] + \frac{Cq_iq_j}{\epsilon_0 r} \qquad \text{for} \quad r < r_c \tag{1}$$

where r is the interatomic length, r_c is the cutoff distance, ϵ_{LJ} is the potential well depth, σ is the characteristic length at which the potential goes to zero, q is the atomic charge, ϵ_0 is the dielectric constant, and C is a constant (all LJ potential parameters are shown in Table 2).

It should be noted that for use with the PPPM solver the Coulomb term includes a damping factor, which goes to zero at r_c, and takes an $erfc$ form. It should also be noted that different cutoff radii (r_c) are used for the LJ and Coulombic terms. The LJ term cutoff is 11.66, while the Coulombic term cutoff is 12.66 ($4\sigma_{\text{oxy}}$). For atoms of different LJ molecules the common Lorentz-Berthelot mixing rules were applied:

$$\sigma_{ij} = \frac{1}{2}(\sigma_i + \sigma_j) \qquad \text{and} \qquad \epsilon_{ij} = \sqrt{\epsilon_i \epsilon_j} \tag{2}$$

In keeping with the SPC/E model, the hydrogen molecules do not have any LJ interactions.

From the initial setup, the simulations were carried out in two phases. Initialization and equilibration took place during Phase I, where an energy minimization was implemented on the initial atom arrangement, after which a 400-ps equilibration occurred. The equilibration occurred in the canonical ensemble (NVT) with a Nosé–Hoover thermostat at 300 K on all atoms. The temperature, vapor pressure, and energy were monitored to ensure equilibrium prior to the beginning of Phase II.

At the start of Phase II, the thermostat is removed from all atoms except those in the second monolayer of the substrate. The temperature of these atoms was increased (instantaneously) to

TABLE 2: LJ potential parameters

LJ Interaction	$\sigma(\text{Å})$	$\epsilon(\text{eV})$	$r_c(\text{Å})$
Cu-Cu	2.3300	0.40960	12.664
Cu-C	3.0825	0.02578	12.664
Cu-O	2.7480	0.05254	12.664
Cu-H	0.0000	0.0000	0.0000
Ni-Ni	2.2800	0.51970	12.664
Ni-C	2.8400	0.60000	12.664
Ni-O	2.7230	0.05918	12.664
Ni-H	0.0000	0.0000	0.0000
Pt-Pt	2.4750	0.52115	12.664
Pt-C	2.9500	0.02206	12.664
Pt-O	2.8205	0.05927	12.664
Pt-H	0.0000	0.00000	0.0000
O-O	3.1660	0.00674	12.664
O-C	3.1900	0.00455	12.664
O-H	0.0000	0.0000	0.0000

400 K to induce nucleate boiling, while all other atoms were held in the microcanonical (NVE) ensemble. Over the course of 3000 ps the high-temperature thermostat atoms were allowed to interact with the upper layers of the substrate, graphene, and water, thereby increasing the overall temperature of the system. Both phases used a velocity-Verlet integration scheme with a 1-fs time step.

Thermal conductivity was calculated using the Green-Kubo method. First, the heat flux J was calculated using the formula

$$J = \frac{1}{V}\left[\sum_{i=1}^{N}(e_i - S_i)v_i\right] \tag{3}$$

where V is the solid volume, e_i is the per-atom energy, S_i is the per-atom stress tensor, and v_i is the per-atom velocity. Then thermal conductivity k can be determined via the ensemble average of the autocorrelation of the heat flux:

$$k = \frac{V}{3k_B T^2}\int_0^\infty \langle J(0)\cdot J(t)\rangle dt \tag{4}$$

where k_B is the Boltzmann constant and T is the temperature. As these simulations utilize classical MD, it should be noted that all conductivities only include the portion due to phonon transport.

In order to gain further insight into the relationship between the substrate, graphene sheet, and liquid water, we calculated the vibrational density of states (VDOS) for these system components. The VDOS is proportional to the Fourier transform of the normalized velocity autocorrelation function (VACF) and can thus be calculated using the following relation:

$$D = \int_{-\infty}^{\infty} \frac{\sum_{i=1}^{N}\langle v_i(t)\cdot v_i(0)\rangle}{\sum_{i=1}^{N}\langle v_i(0)\cdot v_i(0)\rangle} \tag{5}$$

where v_i is the velocity of the i_{th} atom, and $\sum_{i=1}^{N}\langle v_i(t)\cdot v_i(0)\rangle / \sum_{i=1}^{N}\langle v_i(0)\cdot v_i(0)\rangle$ is the normalized VACF.

In order to better compare the VDOS data we calculated a quantity S, the overlap of the vibration spectra:

$$S = \frac{\int_0^\infty D_1(f)D_2(f)df}{\int_0^\infty D_1(f)df \int_0^\infty D_2(f)df} \tag{6}$$

where D_1 and D_2 are two different VDOS profiles. Two overlaps were calculated for each case, between the substrate and water (S_{SW}), and graphene and water (S_{GW}).

3. RESULTS AND DISCUSSION

In general, the metal-graphene substrates all increase in temperature very quickly after the onset of Phase II, reaching the target temperature within 30 ps. The SiG substrate requires a bit more time, taking more than 650 ps to reach 400 K. There is very little separation between the water temperatures of different plane cases for all but the SiG substrate, in which the 111 plane reaches the target temperature within 600 ps of heating, while the other planes require 1100 ps. It should be noted that the temperature overshoot in the SiG cases was $\sim$ 7%–12%, compared to only $\sim$ 5% for the metal-graphene cases.

Figure 2 shows the through-plane thermal conductivity for each substrate as heat is provided in the z direction, along with reference values for validation purposes. The bottom bar graph shows the conductivity for different planes of each pure substrate, while the top shows the overall SLG-coated substrate conductivity for the 100 plane as well as typical graphene-only conductivities. Starting at the bottom of the figure, Cu has shown 2%–10% phonon contribution to the total thermal conductivity (400 W/mK) in previous works (Momenzadeh et al., 2013; Yao et al., 2017), which aligns well with the present results shown ($\sim$ 2.5%–9.5% phonon contribution). Momenzadeh et al. (2013) calculated Cu conductivity via the MD/Green-Kubo method at zero pressure (and using an EAM potential), while Yao et al. (2017) experimentally determined low-temperature (< 60 K) phonon conductivity in single-crystal Cu by suppressing electronic thermal conduction via magnetic field. Ni (bulk $k \sim 90$ W/mK) shows 8%–30% phonon contribution, which is somewhat higher than the previous work by Ou et al. (2008), which found $\sim$ 3% phonon contribution at 300 K by using Ni nanowire and estimating phonon conductivity from resistivity measurements and the Wiedemann-Franz law. However, boundary scattering effects in the nanowire could explain their lower conductivity values. There is good agreement with Heino and Ristolainen (2003), who used MD to apply a constant heat flux (in the 100 direction), measuring the temperature gradient, then directly calculated the conductivity. Pt (bulk $k \sim 71$ W/mK) shows 3%–28% phonon contribution, which is also in good agreement with Heino and Ristolainen (2003) ($\sim$ 15% phonon contribution). Si (bulk $k \sim 145$ W/mK), which has a very large phonon contribution, has a thermal conductivity ranging from $\sim$ 6 to 11 W/mK, lower than that found by Esfarjani et al. (2011), which used the MD/Green-Kubo method at 600 K and resulted in conductivities of 27–47 W/mK.

The single-layer graphene sheet, as expected, has a through-plane thermal conductivity greater (by one to two orders of magnitude) than that of the metallic and semiconductor substrates studied. Typical values of the 100 plane (labeled "SLG") are shown in the top of Fig. 2.

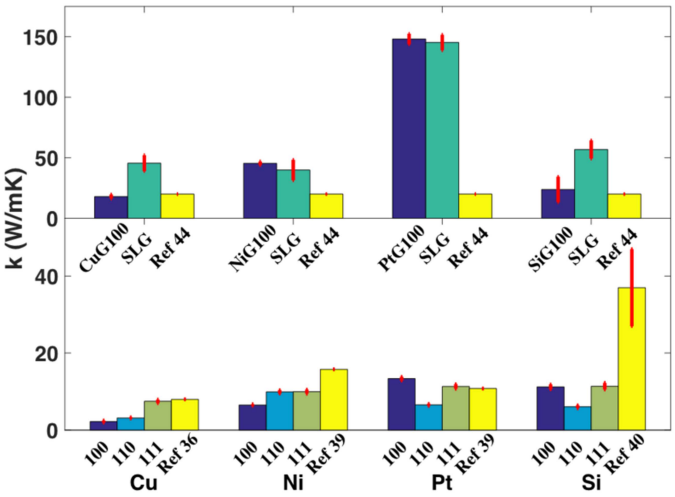

FIG. 2: Thermal conductivity values for the different substrate planes (bottom) as well as graphene only and SLG-coated substrates (top), with error bars shown in red

The graphene-only k values ranged from 13 to 200 W/mK, which is much lower than found in previous studies (Evans et al., 2010; Nika et al., 2009), though these measured the in-plane conductivity of free (suspended) SLG. Also, supported graphene has lower thermal conductivity in part due to damping of out-of-plane phonon modes (Ong and Pop, 2011; Seol et al., 2010). The k values presented here represent the through-plane conductivity, and as graphene is an anisotropic 2D material this tends to be much lower than its in-plane conductivity (Nika et al., 2009; Ong and Pop, 2011). Indeed, in our study the in-plane conductivity (not shown) was found to be anywhere from one to three orders of magnitude greater than the through-plane conductivity. For comparison, results from Alofi and Srivastava (2013) (of through-plane graphite conductivity) are presented with our data. We expect this to be of the same order of magnitude as graphene through-plane conductivity. The SLG-substrate conductivity for the 100 planes is shown in dark blue. In all cases they are higher than that of the bare substrate, and in the 100- and 110-plane cases they are either within the margin of error or below the values of the SLG conductivity. Curiously, the conductivity values for the 111-plane SLG substrates (not shown) are all greater than the SLG-only values. Further exploration is required to determine the exact cause; however, it is possible that the combination of Si's diamond lattice and 111 plane results in better coupling between materials, resulting in a reduction of cross-plane phonon scattering. There was no obvious trend regarding specific lattice planes (100, 110, etc.) having higher or lower conductivities, but it is clear that the addition of graphene greatly improves overall k values. The PtG100 case showed the largest overall combined conductivity, averaging just above 148 W/mK.

Figure 3 shows some typical thermal conductivity profiles for SLG-coated substrates during Phase II. Generally, there is a brief period (0.5–1.5 ns) of transience after the temperature is increased at the beginning of the phase, after which conductivity values become relatively stable.

Figure 4 shows Phase II heat flux profiles for the SLG substrates (110 plane) in order to highlight the overall trends. As mentioned, there is a heat flux peak reached very soon (within

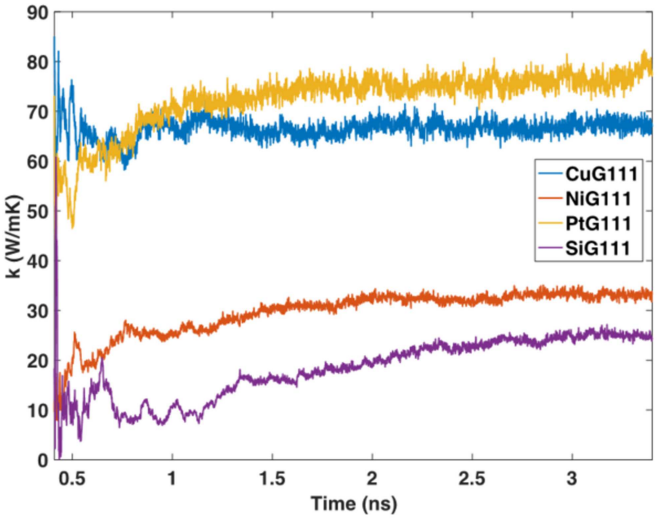

FIG. 3: Phase II thermal conductivity profile for select SLG-coated substrates

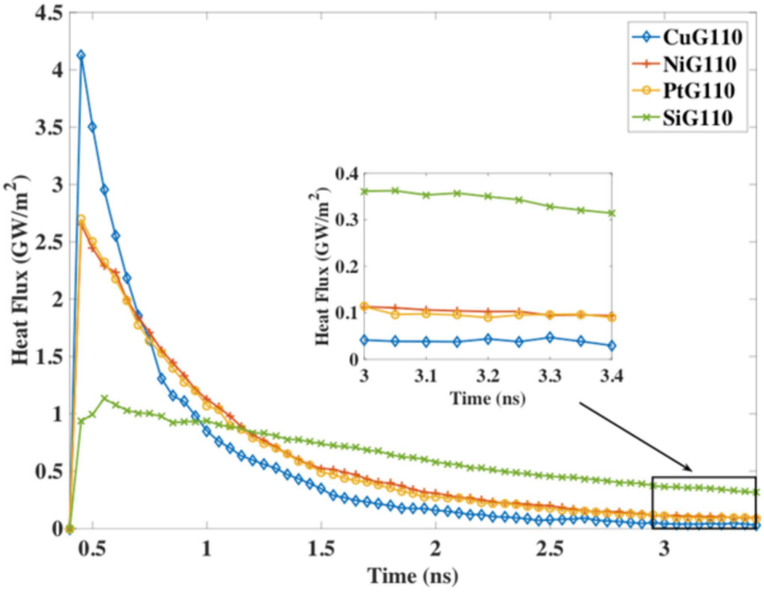

FIG. 4: Heat flux profile for SLG-coated substrates. Inset shows values at the end of the simulation.

0.2 ns) after the onset of Phase II, followed by an exponential decay as the temperature equalizes. At around 3 ns the flux values tend to reach stable levels with respect to time, as well as in relation to one another.

Figure 5 details the heat flux profiles for each case. The fluxes shown represent running average values based on the total energy increase of the water from the beginning of Phase II. Results from additional grapheneless simulations (water was heated directly on the 100 plane of the metal and Si substrates) were also included for comparison. For the CuG, PtG, and SiG substrates the initial profile had distinct maxima in the first 50–100 ps, with $\sim$ 1–2 GW/m^2 difference between peaks (shown in the bottom of the figure). The 110, 111, and 111 planes resulted in the highest peaks, respectively. Of the graphene-containing cases, CuG110 resulted in a maximum overall peak of 4.50 GW/m^2, while SiG110 had the lowest peak of 1.58 GW/m^2. However, perhaps the most surprising result is that for all materials the grapheneless substrates had much higher initial peaks than the others, ranging from $\sim$ 4 to 14 GW/m^2. The interfacial thermal (Kapitza) resistance between the graphene and substrate layers could play a role in this effect, reducing heat transfer between solid layers as well as graphene-water layers (Alexeev et al., 2015). The single-layer nature of the graphene would also play a role, as the thermal conductance of graphene tends to increase with the number of layers (Chang et al., 2012). This overall trend goes against previous experimental works (Jaikumar et al., 2017; Seo et al., 2015), which showed an increase in heat flux with the addition of a graphene coating. However, it should be noted that in those experiments, the resulting graphene surfaces have increased surface roughness compared with the plain substrates, as well as multiple graphene layers, both of which could act to increase heat flux over the bare substrate cases. These millimeter-scale experiments showed overall heat fluxes on the order of 1 MW/m^2, three to four orders of magnitude lower than found in our nanoscale simulations.

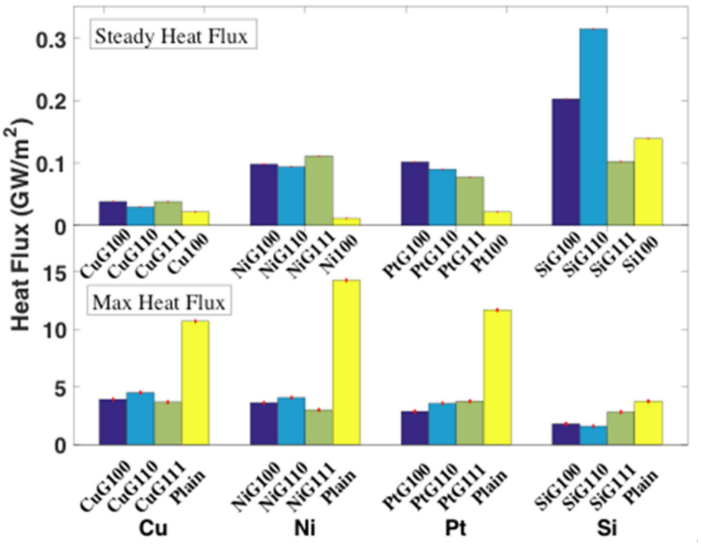

FIG. 5: Heat flux values for different substrate cases, with error bars shown in red.

In general, however, the initial peak would only be of interest in applications with extremely short durations, as the peak effects subside within 1.5–2.5 ns of the temperature increase. After this point the heat fluxes reach relative levels that remain the same for the remainder of the simulation. For example, for the PtG substrate, after $\sim$ 2.5 ns the 100 plane exhibits the highest flux, followed by the 110 and 111 planes, and this remains the case until the end of the simulation. Thus, for longer heat transfer processes the stable flux values (top of figure) would be of greater interest. In all cases, after the initial peak the heat flux decreased exponentially toward a steady state value with less separation between cases. By the end of Phase II separation between maximum and minimum cases typically ranged between $\sim$ 0.02 and 0.20 GW/m^2. It should be noted that among graphene-containing cases the maximum initial peak did not predict the maximum average values at the end of the simulation; in fact the opposite appears to be true. The cases exhibiting the highest initial peaks tended to have the lowest average heat flux values. Also, the (grapheneless) Cu, Ni, Pt, and Si100 cases moved from having the highest initial peaks to either the lowest or next-to-lowest fluxes averaged over the entirety of Phase II. The CuG100 and CuG111 stable fluxes were 1.7 $\times$ greater than that of Cu100, while NiG111 was 9.6 $\times$ greater than Ni100. PtG100 shows a 4.7 $\times$ increase over Pt100, while SiG110 is 2.3 $\times$ greater than Si100. Of the SLG-substrate cases, SiG110 resulted in the highest average heat flux value ($\sim$ 0.31 GW/m^2), while CuG110 had the lowest ($\sim$ 0.03 GW/m^2). This general trend does follow the experimental data. Due to graphene's superior conductivity the initial Kapitza resistance is overcome and allows SLG-coated substrates to have better heat flux performance than grapheneless substrates once a steady heat flux is achieved.

Based on Fourier's law of heat conduction, Fig. 6 details the temperature gradient for an SLG-substrate case (CuG100) and a grapheneless case (Cu100) from the known conductivity and heat flux profiles. As can be seen, the dT/dz values for the SLG substrate are lower than that of the grapheneless case, especially in the first half of Phase II. Although its through-plane conductivity is poor, graphene's high in-plane thermal conductivity allows for more uniform

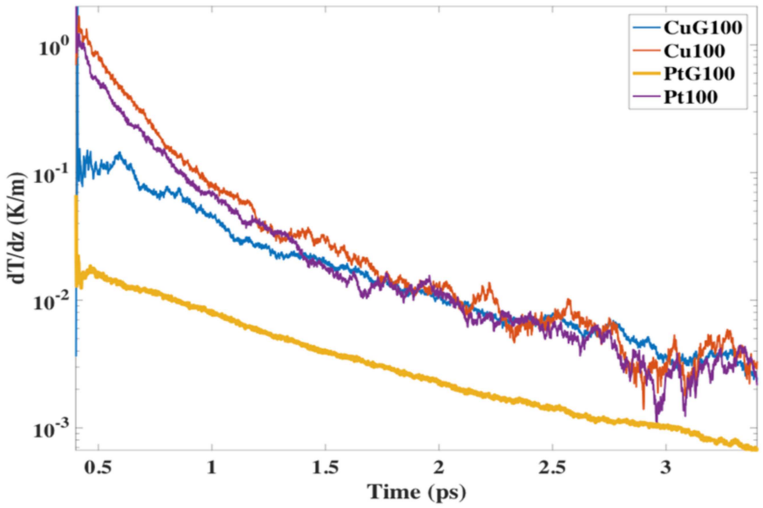

FIG. 6: Time-averaged Phase II temperature gradient data for select cases (log-scale).

heating. In practical terms, this much less steep temperature gradient results in a reduction of hot spots, thereby preventing overheating of the substrate. Later in the simulation, once the water temperature has had a chance to increase via conduction, the gradient of the grapheneless case is much closer to that of the SLG substrate, though still $\sim 2\times$ larger. Although not shown, the dT/dx and dT/dy gradients show the same trend, but with even larger differences in the first half of the simulation.

The nanoscale boiling curves for select substrates were plotted in Fig. 7(a) and Fig. 7(b) to give a sense of the boiling process and CHF trends. To obtain the curves separate simulations were run, where after the Phase I equilibration process the temperature was incrementally raised from 373 to 473 K over 3.5 ns. The temperature of the substrate was raised to various temperatures between 373 and 433 K and each kept steady for 500 ps before moving to the next temperature. An interpolated curve was included for each data set to guide the eye. As could be predicted from the steady heat flux values of Fig. 5, the SLG cases generally show higher heat fluxes than the grapheneless cases. The CHF for the Cu100 is ~ 0.31 GW/m^2, while the CuG100 CHF is ~ 0.36 GW/m^2, an increase of $\sim 14\%$. Also, the CHF is seen to occur earlier in the SLG case, at 20 K superheat compared to the 25 K superheat required for the grapheneless case. The PtG100 case (~ 0.48 GW/m^2) shows a $\sim 9\%$ increase in CHF over that of Pt100 (~ 0.43 GW/m^2). In this case, where both substrates have similar CHF values, the same superheat is required. Taking both the Cu and Pt cases together and because the heating surface is almost perfectly flat (so nanoscale roughness does not come into play), this suggests that larger CHF values will occur at lower superheat due to better heat transfer, which can vaporize the liquid and bring about film boiling more quickly. In general, the conductivity enhancement due to the SLG coating allows better overall heat transfer, which follows the trends in Fig. 5 and previous experiments (Jaikumar et al., 2017; Seo et al., 2015). After CHF is reached, the flux drops briefly before continuing to rise again during film boiling.

All S values, which measure the degree of VDOS overlap, are detailed in Table 3. Perhaps unsurprisingly, in all cases SSW had the highest overlap value. Again, due to the hydrophobicity

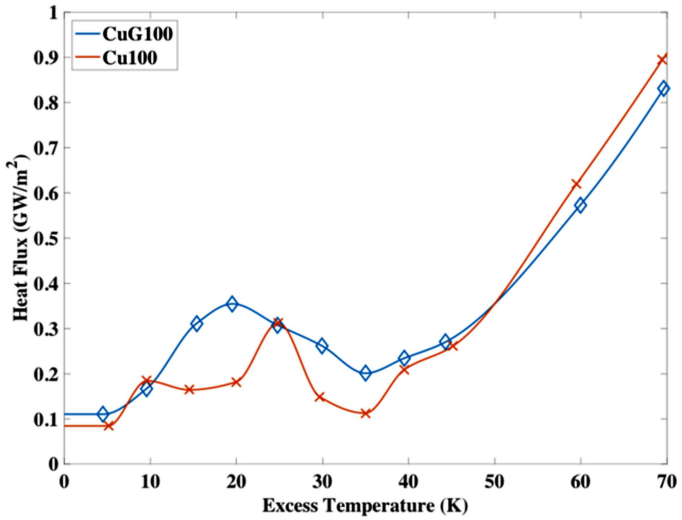

(a)

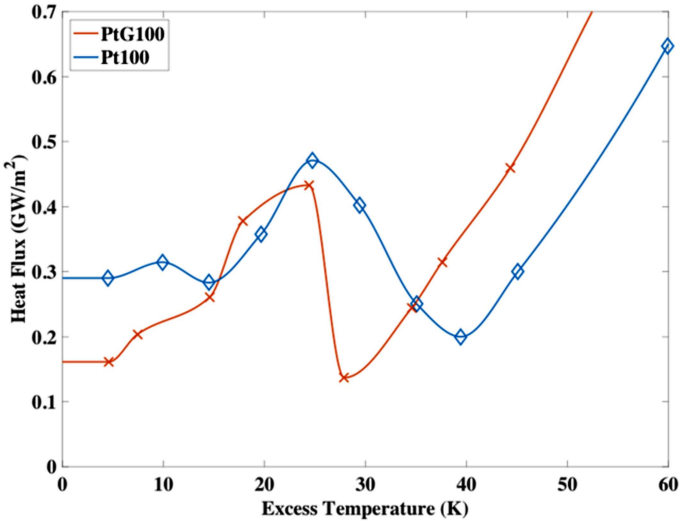

(b)

FIG. 7: Time-averaged Phase II temperature gradient data for select cases (log-scale)

of graphene the substrates tend to interact more strongly with the liquid, which improves vibration spectra overlap. Although graphene can improve conductivity, it still has a weak correlation with water, which may hinder overall heat transfer somewhat.

In order to determine whether the VDOS overlap correlated with better heat transfer, the heat flux values were plotted against the ratios of the overlap values, shown in Fig. 8. In particular, the ratios SGW/SSW were chosen (the raw S values were also plotted against the heat flux,

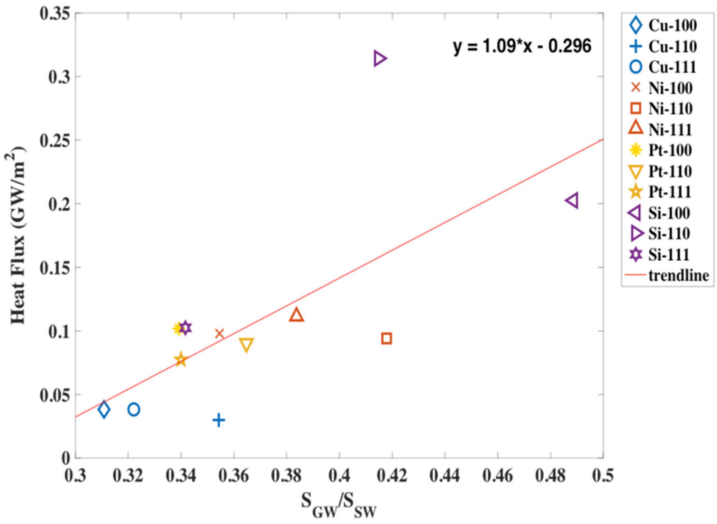

FIG. 8: Steady heat flux vs. overlap ratio SGW/SSW.

but no significant correlation was found), as these ratios can perhaps give a good view of the mismatch between substrates. The ratios for all cases range between ~ 0.3 and 0.5, suggesting a certain amount of mismatch, and thus Kapitza resistance, is always present. The only type of adsorption present in the simulations is physisorption, it is assumed that the stronger and more stable chemisorption bonding would result in smaller Kapitza resistance (Alofi and Srivastava, 2013), higher overlap ratios, and higher heat flux. The figure shows the steady flux values at the end of our simulation (with a trendline to guide the eye) and shows a positive correlation. This positive correlation makes intuitive sense, since an increase in the overlap ratio (while < 1)

TABLE 3: Boiling curves for (a) CuG100 and Cu100, and (b) PtG100 and Pt100

Case	SSW	SGW	SGW/SSW
CuG100	0.5015	0.1559	0.3109
CuG110	0.5808	0.2058	0.3544
CuG111	0.6486	0.2089	0.3221
NiG100	0.6224	0.2206	0.3545
NiG110	0.5441	0.2273	0.4178
NiG111	0.6202	0.2379	0.3837
PtG100	0.6082	0.2063	0.3392
PtG110	0.5675	0.2070	0.3648
PtG111	0.6302	0.2144	0.3401
SiG100	0.4467	0.2183	0.4887
SiG110	0.5265	0.2184	0.4149
SiG111	0.5415	0.1850	0.3417

implies less thermal resistance (between graphene and water) and more efficient heat transfer. At higher liquid temperatures, higher-frequency graphene modes (which also have a somewhat higher VDOS) are better coupled to the water and play a larger role in heat transfer, as opposed to the lower-frequency modes which dominate when the spectral temperature is closer to that of the adjacent liquid or solid (Mao et al., 2013).

Figures 9(a) and 9(b) detail the liquid water density profiles during Phase II for Cu and Ni, and Pt and Si substrates, respectively. In order to calculate the density, the simulation domain was sliced into 1-Å-high slabs, running the entire x and y directions. The density of each slab was then averaged every 5000 time steps for the duration of the simulation. The density values presented were averaged over the entire duration of the phase. Only the first 20 Å are shown

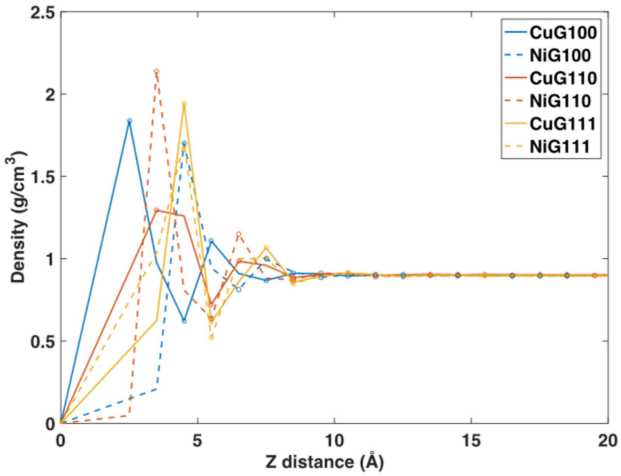

(a)

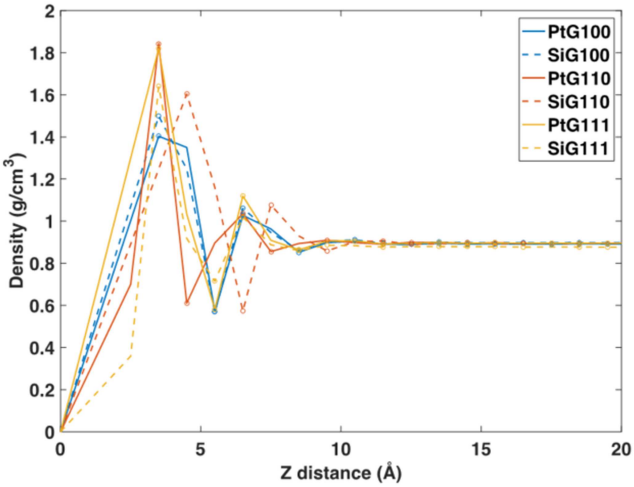

(b)

FIG. 9: Phase II density profile for liquid water over (a) CuG and NiG, and (b) PtG and SiG substrates.

in order to better view the density stratification near the solid wall. It should be noted that the oscillatory behavior of the density near the graphene sheet is due to the expected stratification due to wall interaction (Alexeev et al., 2015), and can be attributed to the orientation of the water molecules closest to the graphene wall, which is determined by the water dipole (Shen et al., 2013). The differences in near-graphene liquid density between the cases can be attributed to the substrate/graphene interaction potentials, substrate lattice constants, and planar densities. In the case of Cu, the CuG111 shows the highest-density peak, while NiG110, PtG110, and SiG111 show the highest-density peaks for their respective substrates, though the Si peaks are closely clustered. The highest overall peak belongs to the NiG110 case, with a value of ~ 2.18 g/cm^3. The second peaks are also closely clustered and do not appear to show significant differentiation, but rather signify the intermediate density region before the bulk density is reached, which in all cases occurs at roughly 10 Å, with a density between 0.90 and 0.91 [3]. For all substrates the density values drop to nearly zero after the liquid/vapor interface, at a height of 40 Å (not shown). The small circles in each figure mark the local maxima and minima in the density values, which were recorded and could be compared to heat flux, thermal conductivity, and vibrational density of states (VDOS) data to look for underlying trends.

4. CONCLUSIONS

In this study molecular dynamics was used to simulate water boiling over a heated solid, which consisted of a substrate topped with a single graphene sheet, in order to enhance boiling heat transfer. The following concluding remarks can be drafted:

1. The addition of single-layer graphene greatly improves the through-plane thermal conductivity of Cu, Ni, Pt, and Si substrates during boiling, with increases in conductivity one to two orders of magnitude greater than that of the substrate alone. The PtG100 case showed the best conductivity, just slightly below 148 W/mK.

2. Density stratification of water was confirmed, with a region of alternating density maxima and minima near the graphene sheet before the bulk density was achieved after ~ 10 Å. The density peak data were correlated with the initial maximum heat flux values, generally predicting higher maximum flux values with increasing density.

3. For cases involving coated graphene, the highest maximum flux value occurred in the CuG110. Bare substrates (without graphene) were also simulated and found to have higher initial peaks, most likely due to reduced Kapitza resistance.

4. Stable heat flux values achieved by the end of the simulation time, however, tended to be higher for the graphene-containing cases, with ~ 2–$10\times$ increases over the plain substrate cases.

5. The temperature gradients for SLG-coated substrates were found to be much lower than grapheneless substrates, especially shortly after the initial temperature rise. This is due to graphene's high thermal conductivity, which allows for more uniform heating.

6. Nanoscale boiling curves were produced, comparing select SLG-coated and grapheneless cases. The CuG100 case showed a 14% increase in CHF (~ 0.36 GMW/m^2) over the Cu100 case, and had higher fluxes in all stages of boiling. PtG100 showed a 9% increase in CHF (~ 0.48 GMW/m^2) over the Pt100 case. The SLG-coated cases also required less superheat to achieve the CHF condition.

7. Using VDOS data, an overlap ratio SGW/SSW was calculated and used to view heat flux trends. The maximum heat flux was found to be inversely proportional to the overlap ratio, suggesting that the initial heat flux peak is largely dictated by the substrate's, and not graphene's, VDOS (and density peak) characteristics. The average heat flux values (for the relatively short simulation times presented in this work) also correlated inversely with the overlap ratio.

8. For all graphene sheet and substrate combinations in this study, no overlap ratio exceeded 0.5.

REFERENCES

Baiser, M. and Briggs, A., Condensation of Steam on Pin-Fin Tubes: Effect of Circumferential Pin Thickness and Spacing, *Heat Transf. Eng.*, vol. **30**, no. 13, pp. 1017–1023, 2009.

Alexeev, D., Chen, J., Walther, J.H., Giapis, K.P., Angelikopoulos, P., and Koumoutsakos, P., Kapitza Resistance between Few-Layer Graphene and Water: Liquid Layering Effects, *Nano Lett.*, vol. **15**, no. 9, pp. 5744–5749, 2015.

Alofi, A. and Srivastava, G.P., Thermal Conductivity of Graphene and Graphite, *Phys. Rev. B*, vol. **87**, 115421, 2013.

Chang, S.W., Nair, A.K., and Buehler, M.J., Geometry and Temperature Effects of the Interfacial Thermal Conductance in Copper– and Nickel–Graphene Nanocomposites, *J. Phys.: Condens. Matter*, vol. **24**, 245301, 2012.

Choi, W., Lahiri, I., Seelaboyina, R., and Kang, Y.S., Synthesis of Graphene and Its Applications: A Review, *Crit. Rev. Solid State Mater. Sci.*, vol. **35**, pp. 52–71, 2010.

Dahal, A. and Batzill, M., Graphene–Nickel Interfaces: A Review, *Nanoscale*, vol. **6**, pp. 2548–2562, 2014.

Diaz, R. and Guo, Z., Molecular Dynamics Study of Wettability and Pitch Effects on Maximum Critical Heat Flux in Evaporation and Pool Boiling Heat Transfer, *Numer. Heat Transf.*, Part A, vol. **72**, pp. 891–903, 2017a.

Diaz, R. and Guo, Z., A Molecular Dynamics Study of Phobic/Philic Nano-Pattering on Boiling Heat Transfer, *Heat Mass Transf.*, vol. **53**, pp. 1061–1071, 2017b.

Esfarjani, K., Chen, G. and Stokes, H.T., Heat Transport in Silicon from First-Principles Calculations, *Phys. Rev. B*, vol. **84**, 085204, 2011.

Evans, W.J., Hu, L., and Keblinski, P., Thermal Conductivity of Graphene Ribbons from Equilibrium Molecular Dynamics: Effect of Ribbon Width, Edge Roughness, and Hydrogen Termination, *Appl. Phys. Lett.*, vol. **96**, no. 20, 203112, 2010.

Gheltaghy, A.M., Saffari, H., Arshadi, S.S., and Tabatabael, S.S., Prediction of Nucleate Pool Boiling on Hydrophilic Surfaces by Considering the Dynamics Contact Angle Effect on Isolated Bubble, *Heat Transf. Res.*, vol. **49**, pp. 423–435, 2018.

Heino, P. and Ristolainen, E., Thermal Conduction at the Nanoscale in Some Metals by MD, *Microelectron. J.*, vol. **34**, pp. 773–777, 2003.

Humphrey, W., Dalke, A., and Schulten, K., VMD: Visual Molecular Dynamics, *J. Mol. Graphics*, vol. **14**, pp. 33–38, 1996.

Jaikumar, A., Kandlikar, S.G., and Gupta, A., Pool Boiling Enhancement through Graphene and Graphene Oxide Coatings, *Heat Transf. Eng.*, vol. **38**, pp. 1274–1284, 2017.

Kubo, H., Takamatsu, H., and Honda, H., Boiling Heat Transfer from a Silicon Chip Immersed in Degrassed and Gas-Dissolved FC-72: Effect by Size and Number Density of Micro-Reentrant Cavities, *J. Enhanced Heat Transf.*, vol. **24**, pp. 269–278, 2017.

Mao, R., Kong, B.D., Gong, C., Xu, S., Jayasekera, T., Cho, K., and Kim, K.W., First-Principles Calculation of Thermal Transport in Metal/Graphene Systems, *Phys. Rev. B*, vol. **87**, 165410, 2013.

Momenzadeh, L., Evteev, A.V., Levchenko, E.V., Belova, I.V., Murch, G.E., and Sohn, Y.H., Phonon Thermal Conductivity of FCC Cu by Molecular Dynamics Simulation, *Defect Diffus. Forum*, vol. **336**, pp. 169–184, 2013.

Morshed, A.K.M.M., Paul, T.C., and Khan, J.A., Effect of Nanostructures on Evaporation and Explosive Boiling of Thin Liquid Films: A Molecular Dynamics Study, *Appl. Phys. A*, vol. **105**, pp. 445–451, 2011.

Nika, D.L., Pokatilov, E.P., Askerov, A.S., and Balandin, A.A., Phonon Thermal Conduction in Graphene: Role of Umklapp and Edge Roughness Scattering, *Phys. Rev. B*, vol. **79**, 155413, 2009.

Ong, Z.Y. and Pop, E., Effect of Substrate Modes on Thermal Transport in Supported Graphene, *Phys. Rev. B*, vol. **84**, 075471, 2011.

Ou, M.N., Yang, T.J., Harutyunyan, S.R., Chen, Y.Y., Chen, C.D., and Lai, S.J., Electrical and Thermal Transport in Single Nickel Nanowire, *Appl. Phys. Lett.*, vol. **92**, 063101, 2008.

Ouyang, T., Chen, Y., Xie, Y., Wei, X.L., Yang, K., Yang, P., and Zhong, J., Ballistic Thermal Rectification in Asymmetric Three-Terminal Graphene Nanojunctions, *Phys. Rev. B*, vol. **82**, 245403, 2010.

Plimpton, S., Fast Parallel Algorithms for Short-Range Molecular Dynamics, *J. Comput. Phys.*, vol. **117**, pp. 1–19, 1995.

Seo, H., Chu, J.H., Kwon, S.Y., and Bang, I.C., Pool Boiling CHF of Reduced Graphene Oxide, Graphene, and SiC-Coated Surfaces under Highly Wettable FC-72, *Int. J. Heat Mass Transf.*, vol. **82**, pp. 490–502, 2015.

Seol, J.H., Jo, I., Moore, A.L., Lindsay, L., Aitken, Z.H., Pettes, M.T., Li, X., Yao, Z., Huang, R., Broido, D., and Mingo, N., Two-Dimensional Phonon Transport in Supported Graphene, *Science*, vol. **328**, pp. 213–216, 2010.

Seyf, H.R., and Zhang, Y., Molecular Dynamics Simulation of Normal and Explosive Boiling on Nanostructured Surface, *J. Heat Transf.*, vol. **135**, 121503, 2013.

Shatto, D.P. and Peterson, G.P., Flow Boiling Heat Transfer with Twisted Tape Inserts, *J. Enhanced Heat Transf.*, vol. **24**, pp. 21–46, 2017.

Shen, M., Schelling, P.K., and Keblinski, P., Heat Transfer Mechanism Across Few-Layer Graphene by Molecular Dynamics, *Phys. Rev. B*, vol. **88**, 045444, 2013.

Stuart, S.J., Tutein, A.B., and Harrison, J.A., A Reactive Potential for Hydrocarbons with Intermolecular Interactions, *J. Chem. Phys.*, vol. **112**, pp. 6472–6486, 2000.

Yao, M., Zebarjadi, M., and Opeil, C.P., Experimental Determination of Phonon Thermal Conductivity and Lorenz Ratio of Single Crystal Metals: Al, Cu, and Zn, *J. Appl. Phys.*, vol. **122**, 135111, 2017.